Microscopy and Microanalysis (2022), **28**, 1649–1663
doi:10.1017/S1431927622000629

Microscopy AND Microanalysis

Original Article

Differences in Collagen Fiber Diameter and Waviness between Healthy and Aneurysmal Abdominal Aortas

Justyna A. Niestrawska[1,a†], Anna Pukaluk[1,a], Anju R. Babu[1,‡] and Gerhard A. Holzapfel[1,2*]

[1]Institute of Biomechanics, Graz University of Technology, Stremayrgasse 16, 8010 Graz, Austria and [2]Department of Structural Engineering, Norwegian University of Science and Technology (NTNU), 7491 Trondheim, Norway

Abstract

Collagen plays a key role in the strength of aortic walls, so studying micro-structural changes during disease development is critical to better understand collagen reorganization. Second-harmonic generation microscopy is used to obtain images of human aortic collagen in both healthy and diseased states. Methods are being developed in order to efficiently determine the waviness, that is, tortuosity and amplitude, as well as the diameter, orientation, and dispersion of collagen fibers, and bundles in healthy and aneurysmal tissues. The results show layer-specific differences in the collagen of healthy tissues, which decrease in samples of aneurysmal aortic walls. In healthy tissues, the thick collagen bundles of the adventitia are characterized by greater waviness, both in the tortuosity and in the amplitude, compared to the relatively thin and straighter collagen fibers of the media. In contrast, most aneurysmal tissues tend to have a more uniform structure of the aortic wall with no significant difference in collagen diameter between the luminal and abluminal layers. An increase in collagen tortuosity compared to the healthy media is also observed in the aneurysmal luminal layer. The data set provided can help improve related material and multiscale models of aortic walls and aneurysm formation.

Key words: aneurysm, collagen fibers, diameter, human abdominal aorta, second-harmonic generation microscopy, waviness

(Received 11 August 2021; revised 10 March 2022; accepted 10 April 2022)

Introduction

The development of an abdominal aortic aneurysm (AAA) is a remodeling process that is triggered both by the degradation and the synthesis of extracellular matrix proteins and leads to the formation of local dilatations, which eventually lead to the rupture of an aortic wall (Niestrawska et al., 2019; Sherifova & Holzapfel, 2019). The most important structural proteins of the extracellular matrix are collagen and elastin, and both play an important role in the mechanical properties of the aortic tissue (Holzapfel & Ogden, 2018; Sherifova & Holzapfel, 2020). Elastin ensures elasticity at lower stretch, whereas collagen determines the tensile strength at higher stretch (Weisbecker et al., 2013; Chow et al., 2014; Schriefl et al., 2015). Collagen, therefore, takes on a decisive role in preventing ruptures (Holzapfel, 2008; Asgari et al., 2022).

While tissue remodeling takes place during the development of an aneurysm, collagen is influenced in terms of content, cross-links, and structure (Tsamis et al., 2013). Although numerous studies have devoted themselves to the analysis of collagen content in AAA, this remains controversial, as an increase (Menashi et al., 1987; Rizzo et al., 1989; Lindeman et al., 2010), no change (Gandhi et al., 1994), or a decrease (Carmo et al., 2002) has been reported. On the contrary, there is an agreement that the number of cross-links in AAAs is increasing (Bode et al., 2000; Carmo et al., 2002; Lindeman et al., 2010). The structural changes observed include the loss of distinction between the layers (Gasser et al., 2012; Niestrawska et al., 2016, 2019), changes in the orientation and dispersion of collagen fibers (Gasser et al., 2012; Niestrawska et al., 2016, 2019), and the decrease in their waviness (Niestrawska et al., 2016) and the increase in the diameter (Niestrawska et al., 2016; Urabe et al., 2016). The available quantified structural data are limited to orientation and dispersion (Gasser et al., 2012; Niestrawska et al., 2016, 2019; Amabili et al., 2021). To advance the understanding of structural changes caused by aneurysm development and to improve material (Holzapfel et al., 2000; Gasser et al., 2006; Holzapfel et al., 2015; Weisbecker et al., 2015; Li et al., 2018; Franchini et al., 2022) and multiscale (Hayenga et al., 2011; Thunes et al., 2018; Dalbosco et al., 2021) modeling of the aortic tissues and the formation of aneurysms, this study provides the measured values for orientation and dispersion as well as for the first time the diameter and waviness of collagen fibers in human abdominal aortas.

In this article, we first give a brief overview of pathological changes in the arterial wall caused by AAA. In the absence of an established method for quantifying the diameter and waviness of collagen fibers in aortic tissues, we provide a background for

[a]The first two authors contributed equally to this work.

[†]Current address: Macroscopic and Clinical Anatomy, Medical University Graz, Harrachgasse 21, 8010 Graz, Austria.

[‡]Current address: Department of Biotechnology and Medical Engineering, National Institute of Technology Rourkela, Rourkela, Odisha 769008, India.

***Corresponding author:** Gerhard A. Holzapfel, E-mail: holzapfel@tugraz.at

Cite this article: Niestrawska JA, Pukaluk A, Babu AR, Holzapfel GA (2022) Differences in Collagen Fiber Diameter and Waviness between Healthy and Aneurysmal Abdominal Aortas. *Microsc Microanal* **28**, 1649–1663. doi:10.1017/S1431927622000629

methods currently used to quantify collagen fibers from other locations, vessels, and nerve fibers. Then we describe the algorithms that we developed for the aortic collagen. Finally, we evaluate and discuss the structural parameters, diameter, waviness, orientation, and dispersion that are measured in healthy and aneurysmal human abdominal aortas.

Background

Pathological Changes in Collagen from AAA

A healthy abdominal aorta consists of three clearly distinguishable layers, namely intima, media, and adventitia, which are all reinforced by collagen of mostly type I and III (Menashi et al., 1987; Rizzo et al., 1989; Bode et al., 2000; Holzapfel, 2008). In the case of an aneurysm, types I and III remain the main collagen types in the aortic wall (Menashi et al., 1987; Rizzo et al., 1989; Bode et al., 2000). In addition, the ratio of type I to type III for the intact wall remains unchanged (3:1), as reported by Rizzo et al. (1989), as well as for the medial layer (2:1), as described by Menashi et al. (1987). On the other hand, Bode et al. (2000) detected newly synthesized type I collagen in the intima and type III in the media. Overall, the change in the collagen content in an aneurysm is still being discussed (Tsamis et al., 2013). An increased collagen content has been reported by Menashi et al. (1987) and Rizzo et al. (1989) and further supported by Lindeman et al. (2010). In contrast, Carmo et al. (2002) suggested a reduced collagen content, and Gandhi et al. (1994) did not detect any changes. Interestingly, an increase in cross-links is generally accepted (Bode et al., 2000; Carmo et al., 2002; Lindeman et al., 2010; Tsamis et al., 2013).

Healthy aortic layers show pronounced collagen structures. Viewed in a longitudinal–circumferential plane (in-plane), the intimal collagen shows a rather isotropic, carpet-like organization, followed by two counter-rotating fiber families in the media oriented in the circumferential direction and two longitudinally oriented fiber families in the adventitia (Schriefl et al., 2012*b*, 2013; Niestrawska et al., 2016; Amabili et al., 2021). A view from a radial–circumferential plane (out-of-plane) shows almost circumferentially oriented fibers without radial components and very little dispersion through the wall thickness (Schriefl et al., 2012*b*, 2013; Niestrawska et al., 2016; Amabili et al., 2021). The aneurysm development influences the structure (and mechanics) of the collagen fibers (Tsamis et al., 2013). Lindeman et al. (2010) reported on a remodeled collagen architecture that no longer behaves like a coherent network. This study with atomic force microscopy cantilevers showed that mechanical forces acting on individual fibers in AAA were no longer distributed over an adventitial tissue.

Niestrawska et al. (2019) carried out biaxial extension tests on aneurysmal tissues and assigned changes in the orientation and dispersion of collagen fibers to changes in the mechanics. A reorientation of the intimal and adventitial collagen has been suggested as the reason for the loss of initial stiffness. Subsequently, isotropically distributed collagen on the abluminal side led to increased compliance. After all, the increased isotropy was associated with rapid stiffening. Previously, Gasser et al. (2012) and Niestrawska et al. (2016) found a loss of the characteristic layer structure, measured the orientation and dispersion of collagen fibers, and reported a higher fiber dispersion out-of-plane in aneurysmal aortic walls. Neither the waviness nor the diameter of the collagen fibers have been quantified so far. Niestrawska et al. (2016) and Urabe et al. (2016) pointed to thicker collagen struts in aneurysmal tissues compared to healthy tissue, while Niestrawska et al. (2016) also documented that the collagen fibers in the abluminal layer of AAAs have lost their waviness.

Quantification of the Fiber Diameter

The diameter of tubular structures, such as fibers or vessels, is assumed to be equal to the thickness of the fiber (or vessel) represented by a projection parallel to its centerline (Pickering et al., 1996; Brightman et al., 2000; Heneghan et al., 2002; Roeder et al., 2002; Wu et al., 2003; Ziabari et al., 2009; D'Amore et al., 2010; Mencucci et al., 2010; Changoor et al., 2011; Chen et al., 2011, 2013; Koch et al., 2014). The perpendicular projection is an alternative; in this case, the diameter of the fiber (or vessel) is the diameter of the projected circle (Almutairi et al., 2015). While the definition is simple, there are several factors that affect the measurement such as the quality of the microscopy images, the angular deviation between the projection plane and the centerline, and the wavy character of the observed structures. The aspects mentioned above could explain the difficulties in establishing automated procedures. However, the usual manual approach to measuring the diameter is supported by image analysis software (Pickering et al., 1996; Brightman et al., 2000; Roeder et al., 2002; Mencucci et al., 2010; Changoor et al., 2011; Chen et al., 2011, 2013). With manual measurement, the operator typically selects two points that define the fiber diameter (i.e. thickness in projection parallel to the centerline of the fiber), measures the distance between these points in pixels, and converts it to micrometers based on the pixel size. Similar techniques have been chosen to assess the diameter of collagen fibers by, for example, Pickering et al. (1996) in human coronary atherosclerotic lesions, Mencucci et al. (2010) in the human cornea, Changoor et al. (2011) in human articular cartilage, or Chen et al. (2011, 2013) in porcine coronary arteries. Similarly, Brightman et al. (2000) and Roeder et al. (2002) assessed collagen scaffolds using images with binarized fibers.

For retinal vessels (Heneghan et al., 2002), collagenous scaffolds (Wu et al., 2003; Ziabari et al., 2009), or soft tissues (D'Amore et al., 2010; Koch et al., 2014), algorithms have been developed that allow diameter measurements in binary images. Heneghan et al. (2002) suggested defining a point in a binarized vessel and drawing line segments that pass through this point for all possible rotations, while all segments were contained within the binarized vessel. The smallest segment was taken as the vessel diameter. Wu et al. (2003) determined the diameter of fibers in collagen matrices with the help of the Euclidean distance transform (Borgefors, 1986). Ziabari et al. (2009) proposed a replacement for the distance transform to study the diameter of electrospun nanofibers. The proposed method comprises drawing a horizontal segment within a fiber, finding the center of that segment, and drawing a vertical segment from that center to the edge of the fiber. The fiber diameter is then calculated based on these segments. Although the authors concluded that their method gave more accurate results, it is worth noting that electrospun nanofibers are straight and this algorithm has not been validated for wavy fibers. D'Amore et al. (2010) combined binarized centerlines with grayscale images to analyze rat collagen scaffolds and carotid arteries. The binarized centerlines were used to select a portion of a fiber between the network nodes. Gray intensity and gray intensity gradient of grayscale images were used to extract a fiber from the background or from a bundle. Koch et al. (2014) chose distance transform again to measure the diameter of fibers in the human thoracic aortas. Unfortunately, the results obtained

https://doi.org/10.1017/S1431927622000629 Published online by Cambridge University Press

were only shown in pixels, so the data cannot be used as a quantitative reference. Nevertheless, the distance transform for our study (see the section "Diameter" for more details) was chosen as a stable and sufficiently fast solution.

Quantification of Fiber Waviness

Numerous metrics of waviness, also known as tortuosity, are proposed in the literature (Dougherty & Varro, 2000; Bullitt et al., 2003; Grisan et al., 2008; Koprowski et al., 2012; Ghazanfari et al., 2015; Annunziata et al., 2016). Bullitt et al. (2003) has listed and compared three of them, namely the distance metric, the inflection count metric, and the sum of angles metric. The distance metric provides a relationship between the actual length of a curve and the linear distance between its end-points. Although commonly used (Heneghan et al., 2002; Rezakhaniha et al., 2012; Fata et al., 2013; Chow et al., 2014; Koch et al., 2014; Zeinali-Davarani et al., 2015), this measure has a significant disadvantage, since it shows the same value for a fiber with a high amplitude and only one inflection point as for a fiber with a low amplitude, but several inflection points. The inflection count metric overcomes this disadvantage by multiplying a value of the distance metric by a number of inflection points. The sum of angles metric is an alternative approach in which the total curvature is integrated along a curve and normalized by the curve length. The latter approach is particularly useful with a three-dimensional helical curve. It has been shown that this metric is able to distinguish between three helices of the same length but variable frequency and amplitude, while neither the distance metric nor the inflection count metric was able to identify their different tortuosities. The distance metric was unsuccessful because of identical lengths and the inflection count metric because of missing inflection points on a helical curve. In contrast, the sum of angles metric performed poorly on a set of three sinusoidal waves with the same frequency but different amplitude, while both the distance metric and the inflection count metric gave satisfactory results, see Bullitt et al. (2003).

Grisan et al. (2008) proposed a measure based on dividing the curve into segments at inflection points, calculating the distance metric for each segment, and finally summarizing all the metrics and their number. This measure was specially developed for retinal vessels and goes well with clinically perceived tortuosity. For large vessels, such as an aorta, Dougherty & Varro (2000) proposed a measurement based on second differences in the coordinates of the vessel centerline, since the distance metric was not sensitive enough for this application. Koprowski et al. (2012) reduced the tortuosity problem to an inclination angle for eye fundus vessels. The Gabor wavelet method (Arivazhagan et al., 2006) was used by Ghazanfari et al. (2015) for the quantification of collagen fibers in sheep explants of tissue-engineered heart valves. A tortuosity index was calculated as one minus the maximum number in the Gabor histogram, which was the histogram of Gabor wavelets with different angles of orientation and wavelengths. However, the detection of fiber tortuosity was limited to images of fibers with a defined orientation and was unsuccessful with randomly distributed fibers. An alternative approach was proposed by Annunziata et al. (2016) for the analysis of corneal nerve fibers. The proposed concept was called definition-free and included multirange context filters in which discriminative multiscale features were learned for specific anatomical objects and diseases. Although promising, this method requires application-specific images with predefined tortuosity at various scales in order to train a regressor.

In summary, it can be said that no single tortuosity metric is able to cope with all applications, since tortuosity has a different character for different anatomical and biological structures. Most advanced techniques require the skeletonization of images to extract centerlines from fibers (Dougherty & Varro, 2000; Bullitt et al., 2003; Grisan et al., 2008; Annunziata et al., 2016). The skeletonization of collagen fibers in microscopic images is very demanding, among other things because of the crossing and overlapping fibers. Therefore, manual fiber tracking and the distance metric have been routinely used to assess collagen waviness in vascular tissues, that is, rabbit common carotid arteries (Rezakhaniha et al., 2012), ovine main pulmonary arteries (Fata et al., 2013), and porcine thoracic aortas (Chow et al., 2014; Zeinali-Davarani et al., 2015). The tracing and the measurements were usually supported by the plug-in NeuronJ (Meijering et al., 2004) from the software ImageJ (Schindelin et al., 2012), as in Rezakhaniha et al. (2012), Chow et al. (2014), and Zeinali-Davarani et al. (2015). Although it was successful in locating the adventitial collagen bundles, the manual method failed in locating the medial collagen fibers (Chow et al., 2014). Chow et al. (2014), therefore, suggested using the fractal analysis as a measure of the fiber waviness. In addition, Koch et al. (2014) proposed an algorithm for automating fiber quantification that involves the segmentation and skeletonization of collagen fibers from the human thoracic aorta. Although it was tested with out-of-plane images of the arterial wall and in-plane images of the adventitia, it did not prove successful with in-plane medial images. To overcome the above limitations, here we recommend tracking just a single wave of collagen fiber and measuring the amplitude and tortuosity with the distance metric (for more details, see the section "Waviness").

Methods

Sample Preparation

Twelve samples of healthy abdominal aortas with non-atherosclerotic intimal thickening (59 ± 7 years old, six females and six males) were collected within 24 h after death (Institute of Pathology, Medical University Graz, Graz, Austria) and stored in 0.9% physiological saline solution at 4°C until imaging. The samples used are those documented in Niestrawska et al. (2016). Ten samples of aneurysmal abdominal aortas (67 ± 7 years old, two females and eight males) were collected during open aneurysm repair (Department of Vascular Surgery, Medical University Graz, Graz, Austria) and stored in Dulbecco's modified Eagle's medium (to preserve a possible thrombus) at 4°C until imaging. The aneurysmal abdominal aortic samples used are those documented in Niestrawska et al. (2019). A rectangular piece approximately 15 × 5 mm was cut from each sample, with the longer edge marking the longitudinal direction of the aorta.

Second-Harmonic Generation Microscopic Imaging

Before recording, all specimens were optically cleared according to Schriefl et al. (2013). First, each specimen was dehydrated with a graded ethanol series. Next, the specimens were immersed in a 1:2 solution of ethanol:benzyl alcohol–benzyl benzoate (BABB) for 4 h and then stored in 100% BABB for at least 12 h. All steps were carried out at room temperature.

Second-harmonic generation (SHG) microscopy imaging was carried out at the Institute of Science and Technology in

https://doi.org/10.1017/S1431927622000629 Published online by Cambridge University Press

Klosterneuburg, Austria, using a setup consisting of a Chameleon Titan Saphir laser (Coherent, Inc., USA) integrated into a TriM Scope II confocal microscope (LaVision BioTec GmbH, Germany). The SHG signal was induced by a laser tuned to 880 nm, and the emitted signal was transmitted from a BP 460/50 emission filter to a detector. A Leica IMM CORR CS2 20× water immersion objective was used to take images of 1024 × 1024 pixels, with a pixel size of 0.5 × 0.5 μm in z-stacks of 5 μm steps.

Quantification of Collagen Fibers

Diameter

The SHG images of the media showed clearly distinguishable fibers, whereas fiber bundles were observed in the adventitia. Following Lindeman et al. (2010), we considered the bundle to be mechanically representative. Thus, the bundle diameter was measured in the healthy adventitia and, if it was pronounced, in the aneurysmal tissue. Otherwise, the fiber diameter was measured as for the healthy media. Since the captured SHG images show fibers and bundles parallel to their centerlines, the diameter of both fibers and bundles was recognized from their thickness, as shown in Figure 1. A script was written with MATLAB commands (The MathWorks Inc., 2021) to efficiently measure the diameter of a single fiber or a bundle of fibers. First, a region of interest was selected for processing because the signal-to-noise ratio varied widely within the image. The following procedure consists of two main parts: image processing, which leads to binarization, and diameter detection of the binary images.

The image processing begins with the contrast increase through intensity adjustment (MATLAB function: *imadjust*) and then with the removal of the impulse noise (*medfilt2*). The contrast is then enhanced by histogram equalization (*histeq*), as described in a similar way by D'Amore et al. (2010) and Koch et al. (2014). The further image processing consists of two pipelines developed for fibers and bundles. A flowchart of the image processing workflow is shown in Figure 2.

The preprocessed grayscale image is converted into a binary image (*imbinarize*) whereby the threshold value for the bundles was calculated using the Otsu method (*global*) and a locally adaptive threshold is used for the fibers (*adaptive*). The structuring element, a disc with a pixel radius, is used to remove objects (*imopen*) and to fill holes (*imclose*) that are smaller than the structuring element. The edge detection (*edge*) is an additional step that is carried out on a grayscale image for fiber processing. The recognized edges are then subtracted from the segmented image. The grayscale image is processed again to obtain regional maxima (*imextendedmax*) that are used as a mask for the segmented image. The mask is applied to identify the brightest objects, that is, objects with the strongest recorded signal.

The diameter of the object of the binary image is recognized by means of the Euclidean distance transform (Borgefors, 1986), see Wu et al. (2003) and Koch et al. (2014). The main disadvantage of the distance transform method is the permanent error of one pixel when the width is an even number. Since the object represents the fiber, the diameter of a fiber is measured as the diameter of the circle inscribed on the fiber, similar to that described by Wu et al. (2003). The circle is defined by the pixel with the maximum value of the distance transform; therefore, the position of the pixel is the position of the center of the circle and the radius is equal to this value. Finally, the operator is shown the grayscale image with inscribed circles, as shown in Figure 3, for confirmation or, alternatively, for rejection.

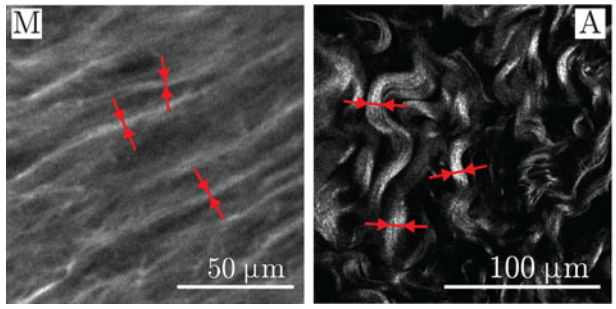

Fig. 1. Representative region of an SHG image showing medial (M) and adventitial (A) collagen of a healthy abdominal aorta. On exemplary medial collagen fibers and adventitial collagen bundles, the thickness, which resembles the diameter, is marked.

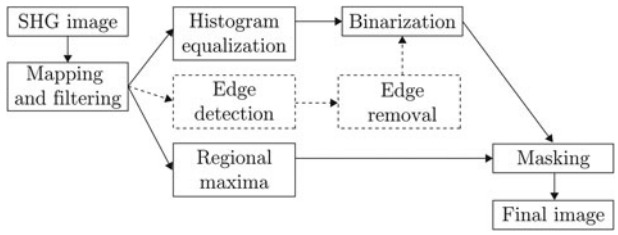

Fig. 2. SHG image processing flowchart: steps that apply to both fibers and bundles are drawn with solid lines, whereas dashed lines indicate additional steps that pertain to fiber processing.

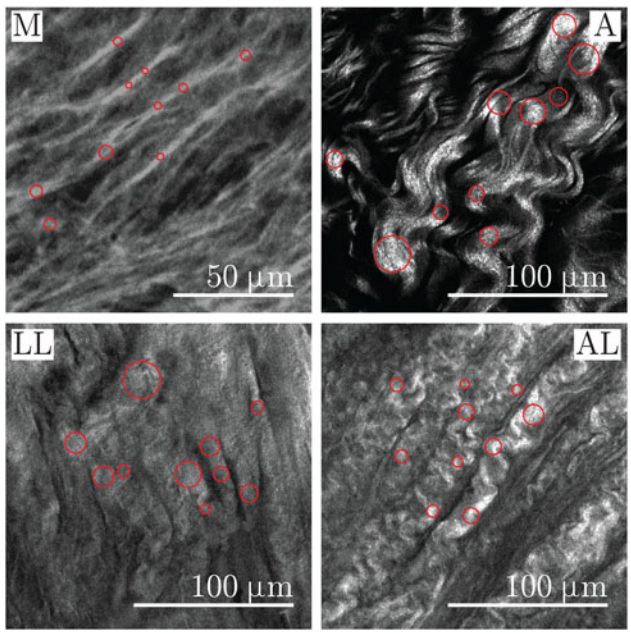

Fig. 3. Close-ups of representative SHG images showing the media (M) and adventitia (A) of healthy aortas as well as the luminal layer (LL) and the abluminal layer (AL) of AAAs. The measurement points of the diameter are visualized as circles in collagen fibers on the media and in bundles of collagen fibers on the adventitia and on the LL and AL of AAA.

The algorithm for image processing and segmentation was validated on sine-wave grating images and on SHG images. As described by Semmlow (2004), the sine-wave grating images were generated with different image sizes, different amplitudes, and number of grating cycles. The images were processed as

https://doi.org/10.1017/S1431927622000629 Published online by Cambridge University Press

previously described, after which the boundary of the segmented image (MATLAB function: *bwboundaries*) was marked on the original sine-wave grating image. The same procedure was applied on all healthy media images and five sets of healthy adventitia. A human operator was involved in judging the boundary recognition, and the boundary recognition was judged to be satisfactory. The diameter detection algorithm was tested on binary images. The rectangular and sine-wave objects of known size and width were generated with MATLAB (The MathWorks Inc., 2021). The detected diameter was, as expected based on the distance transform method used, within one pixel error.

Waviness

The most common definition of tortuosity, as described in the section "Quantification of Fiber Waviness," assumes that an entire collagen fiber is visible from one end to the other in an image. However, we could not clearly distinguish the beginning and end of single fibers as they may not be in the same image. We, therefore, ask when studies on aortic collagen tortuosity identified the respective beginning and end in SHG images. Note that tortuosity does not distinguish between a high-amplitude fiber and only one inflection point and a low-amplitude fiber but multiple inflection points, as we explained in detail in the section "Quantification of Fiber Waviness."

Therefore, we define tortuosity using a single wave of collagen fiber, as shown in Figure 4 (Towler, 2017), and calculate tortuosity T as

$$T = L_f / L_0, \tag{1}$$

where L_0 denotes the end-point-distance and L_f the arc length, similar to the study by, for example, Heneghan et al. (2002). The higher the value of T the more wavy the measured fiber. In addition, we calculated a straightness parameter S as

$$S = 1/T, \tag{2}$$

to match the results obtained with the findings of Rezakhaniha et al. (2012).

Tortuosity alone is not enough to characterize the waviness of a fiber, since fibers with large amplitudes and small end-point-distances can have values similar to fibers with small amplitudes and larger end-point distances. Therefore, we also measured the peak-to-peak amplitude A of a single wave of a collagen fiber, as shown in Figure 4. The software ImageJ (Schindelin et al., 2012) with the plugin NeuronJ (Meijering et al., 2004) was used and combined with MATLAB (The MathWorks Inc., 2021). Here, NeuronJ was used to track the individual waves of collagen fibers or bundles. Representative examples of tracking different layers can be found in Figure 5. A custom-made MATLAB script used the curves from NeuronJ and calculated both the amplitudes A and the tortuosities T. Note that straight fibers do not have clear end-points. As a result, the end-point distance of straight fibers cannot be clearly defined and compared with the end-point distance of wavy fibers. The tortuosity measurement is not influenced, however, since both L_f and L_0 have the same value in straight fibers.

Orientation and Dispersion

The orientation and dispersion of collagen fibers were analyzed according to Schriefl et al. (2012*a*, 2013), Niestrawska et al. (2016), and Holzapfel et al. (2015). Briefly, a combination of Fourier power spectrum analysis and wedge filtering was used to obtain discrete angular distributions with a resolution of 1° relative intensities corresponding to the fiber orientation. The fiber orientations obtained were fitted to the von Mises distribution for the probability density by means of the maximum likelihood estimation, independently for in-plane (ρ_{ip}) and out-of-plane (ρ_{op}), that is,

$$\begin{aligned} \rho_{ip}(\Phi) &= \frac{\exp\left[a\cos 2(\Phi \pm \alpha)\right]}{I_0(a)}, \\ \rho_{op}(\Theta) &= 2\sqrt{\frac{2b}{\pi}}\frac{\exp\left[b(\cos 2\Theta - 1)\right]}{\mathrm{erf}(\sqrt{2b})}, \end{aligned} \tag{3}$$

where $\Phi \in [0, 2\pi]$ and $\Theta \in [-\pi/2, \pi/2]$ represent the general in-plane and out-of-plane fiber directions, respectively, α is the

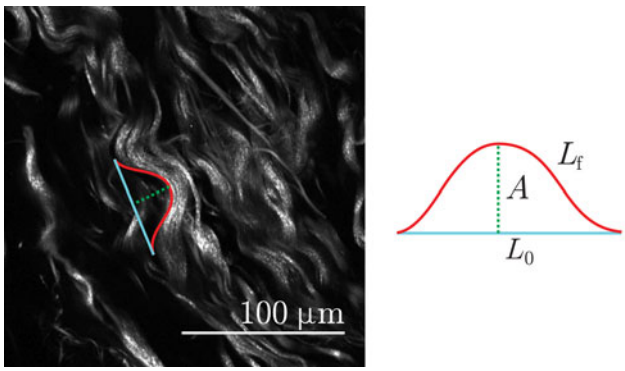

Fig. 4. Representative region of a SHG image showing adventitial collagen from a healthy abdominal aorta. Definitions for the peak-to-peak amplitude A (green dotted line), the end-point-distance L_0 (blue solid line), and the arc length L_f (red curve) are shown for a single wave measured from peak to peak.

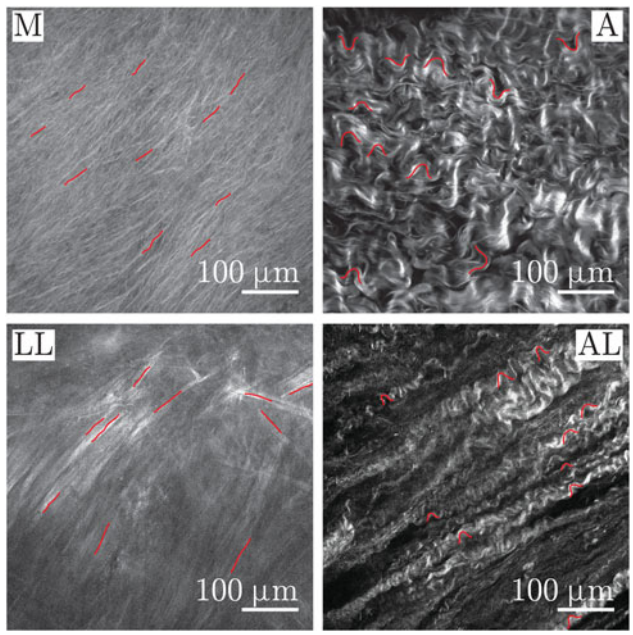

Fig. 5. Representative SHG images showing the tracing in red. Tracing performed on the media (M) and adventitia (A) of healthy aortas as well as the LL and the AL of AAAs. Note that the structure of the AAA layers varied from sample to sample.

https://doi.org/10.1017/S1431927622000629 Published online by Cambridge University Press

mean in-plane fiber direction, a and b are concentration parameters, and $I_0(a)$ is the modified Bessel function of the first kind of order 0. In addition to the in-plane angle α between the mean fiber direction and the circumferential direction of the aorta, the quantities of the fibers dispersion κ_{ip} and κ_{op} for in-plane and out-of-plane were defined as

$$\kappa_{ip} = \frac{1}{2} - \frac{I_1(a)}{2I_0(a)}, \quad \kappa_{op} = \frac{1}{2} - \frac{1}{8b} + \frac{1}{4}\sqrt{\frac{2}{\pi b}}\frac{\exp(-2b)}{\mathrm{erf}(\sqrt{2b})}, \tag{4}$$

where both κ_{ip} and κ_{op} range from 0 for the perfect alignment of the fibers to 1/2 for equally distributed fibers (isotropy) (Holzapfel et al., 2015).

Statistics

To quantify the waviness and the diameter, ten representative images per layer were selected for the analysis and ten measurements per image were recorded and averaged. The orientation and dispersion parameters were calculated from the z-stack images of each layer. The values of the parameters obtained are given as medians together with the first and third quartiles $[Q_1; Q_3]$. The Spearman rank correlation coefficient was used to perform regression analysis to test possible correlations between the parameters. Parameter differences between the aortic layers were evaluated with the Mann–Whitney U test and were considered statistically significant if the p-value was less than 0.05, which corresponds to a confidence of 95%.

The distributions of the parameters tortuosity, straightness, amplitude, and diameter were visualized by means of a probability histogram that contains all measurements for each parameter. In addition, numerous distributions, including extreme value, generalized extreme value, beta (only for straightness parameters), gamma, log-normal, and log-logistic, were fitted to the measured data. The probability density function for the extreme value distribution f was taken to be

$$f(x \mid \mu, \sigma) = \sigma^{-1}\exp\left(\frac{x-\mu}{\sigma}\right)\exp\left[-\exp\left(\frac{x-\mu}{\sigma}\right)\right], \tag{5}$$

where μ is the location parameter and σ is the scaling parameter. The generalized extreme value distribution, which also contains a shape parameter $k \neq 0$, is defined as

$$f(x \mid k, \mu, \sigma) = \sigma^{-1}\exp\left[-\left(1+k\frac{x-\mu}{\sigma}\right)^{-1/k}\right]\left(1+k\frac{x-\mu}{\sigma}\right)^{-1-1/k}, \tag{6}$$

for

$$1 + k\frac{x-\mu}{\sigma} > 0. \tag{7}$$

The beta probability distribution was only fitted to the straightness parameter because it is defined between 0 and 1 (this condition is not fulfilled by other parameters) as

$$f(x \mid \alpha, \beta) = \frac{1}{B(\alpha, \beta)}x^{\alpha-1}(1-x)^{\beta-1}, \tag{8}$$

where α and β are shape parameters, and $B(\alpha, \beta)$ is the beta function defined as

$$B(\alpha, \beta) = \int_{t=0}^{1} t^{\alpha-1}(1-t)^{\beta-1}\,dt. \tag{9}$$

The gamma distribution is defined as

$$f(x \mid \alpha, \beta) = \frac{1}{\beta^{\alpha}\Gamma(\alpha)}x^{\alpha-1}\exp\left(\frac{-x}{\beta}\right), \tag{10}$$

where α is the shape parameter, β is the scaling parameter, and $\Gamma(\alpha)$ is the gamma function according to

$$\Gamma(x) = \int_{t=0}^{\infty}\exp(-t)t^{x-1}\,dt. \tag{11}$$

The probability density function of the log-normal distribution for $x > 0$ is defined as

$$f(x \mid \mu, \sigma) = \frac{1}{x\sigma\sqrt{2\pi}}\exp\left[\frac{-(\log x - \mu)^2}{2\sigma^2}\right], \tag{12}$$

where μ corresponds to the mean of logarithmic values and σ to the standard deviation of the logarithmic values. Taking into account the log-logistic distribution, it is defined for $x \geq 0$ as

$$f(x \mid \mu, \sigma) = \frac{1}{\sigma x}\frac{\exp z}{(1+\exp z)^2}, \tag{13}$$

where μ is the mean of the logarithmic values, σ is the scaling parameter of the logarithmic values, and

$$z = \frac{\log x - \mu}{\sigma}. \tag{14}$$

All statistical analyses were performed in MATLAB (The MathWorks Inc., 2021) including the "Distribution Fitter app", which offers a visual, interactive approach to fitting univariate distributions to data. The distributions used correspond to the MATLAB documentation (The MathWorks Inc., 2021), and the interested reader is referred to Johnson et al. (1994*a*, 1994*b*). The distributions were fitted using the maximum likelihood estimation (Myung, 2003), which provides log-likelihood, mean, variance, and estimated parameters.

The evaluation of the provided fits was supported by probability plots (Chambers et al., 2018), as in Rezakhaniha et al. (2012). This graphical technique is based on the reference line of the analyzed distribution, against which the measurement data are plotted. If the measurement data follow the reference line, they also follow the analyzed distribution. Consequently, deviations of the measurement data from the reference line indicate deviations from the analyzed distribution.

Results

All samples collected were imaged; however, not all images recorded were of sufficient quality for further processing. Therefore, images from two adventitias and four luminal layers were discarded.

Collagen Diameter

The medial layer has the smallest fiber diameter, $D_M = 3.0\,\mu$m [2.6; 3.6]. The bundles of the adventitial fibers have a diameter

https://doi.org/10.1017/S1431927622000629 Published online by Cambridge University Press

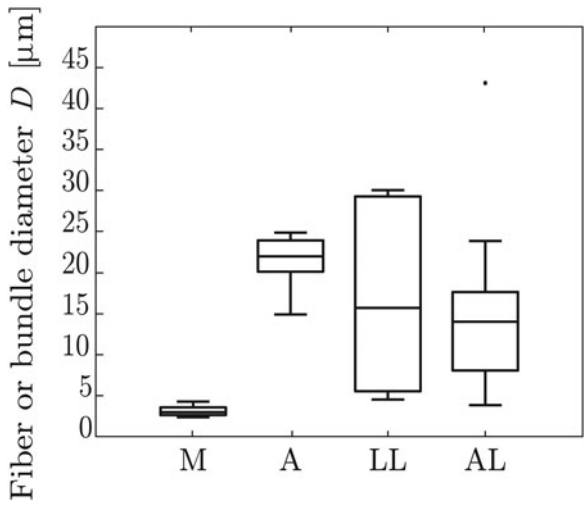

Fig. 6. Box-and-whisker plots for the diameter of fibers or bundles for the healthy media (M) and the healthy adventitia (A) as well as the LL and the AL of AAAs.

of $D_A = 21.9\,\mu m$ [20.2; 23.9]. Both luminal, $D_{LL} = 15.7\,\mu m$ [5.3; 29.3], and abluminal, $D_{AL} = 14.0\,\mu m$ [8.1; 17.7], layers consist either of fibers or bundles. A summary in the form of box-and-whisker plots is shown in Figure 6, whereas the distributions are shown in Figure 7. All diameter data are summarized in Table 1. The Mann–Whitney U test showed a statistically significant difference with $p < 0.001$ for the media tested versus all other layers. The adventitia showed a statistically significant difference compared to the abluminal layer of AAAs ($p = 0.03$), but no significant difference to the luminal layer was seen ($p = 0.43$). In addition, there was no statistically significant difference between the luminal and abluminal layers ($p = 0.79$).

The generalized extreme value and the log-normal distributions provided reasonable fits to the measured data, as shown in Figure 7. The parameters of the distribution fits are summarized in Tables 2 and 3. Based on the probability plots, the generalized extreme value distribution provided a slightly better fit compared to the log-normal distribution. In the generalized extreme value distribution, only outliers with high diameter values deviate from the reference line, as can be observed in Figure 8 for data from the adventitia and the abluminal layer (only two representative examples are shown here). On the other hand, the infinite variance of the generalized extreme value distribution for the luminal layer discourages using this distribution for that particular layer. At this point, it should be noted that the selection of a single distribution that can represent all layers and thus enables a comparison between them is not trivial and requires a compromise in the goodness of fit of individual layers (this note also applies to the distribution fit for the waviness parameters).

Collagen Waviness

Figure 9 shows box-and-whisker plots for (a) the tortuosity T and (b) the amplitude A of the media and the adventitia of healthy tissues and the luminal and abluminal layers of AAAs. The healthy media showed a tortuosity of $T_M = 1.02$ [1.02; 1.02] with an amplitude of $A_M = 2.5\,\mu m$ [2.3; 2.8]. The healthy adventitia had a higher tortuosity of $T_A = 1.41$ [1.33; 1.48] and an amplitude of $A_A = 14.3\,\mu m$ [13.3; 15.6]. Media and adventitia showed significantly different values for both tortuosity ($p < 0.001$) and amplitude ($p < 0.001$).

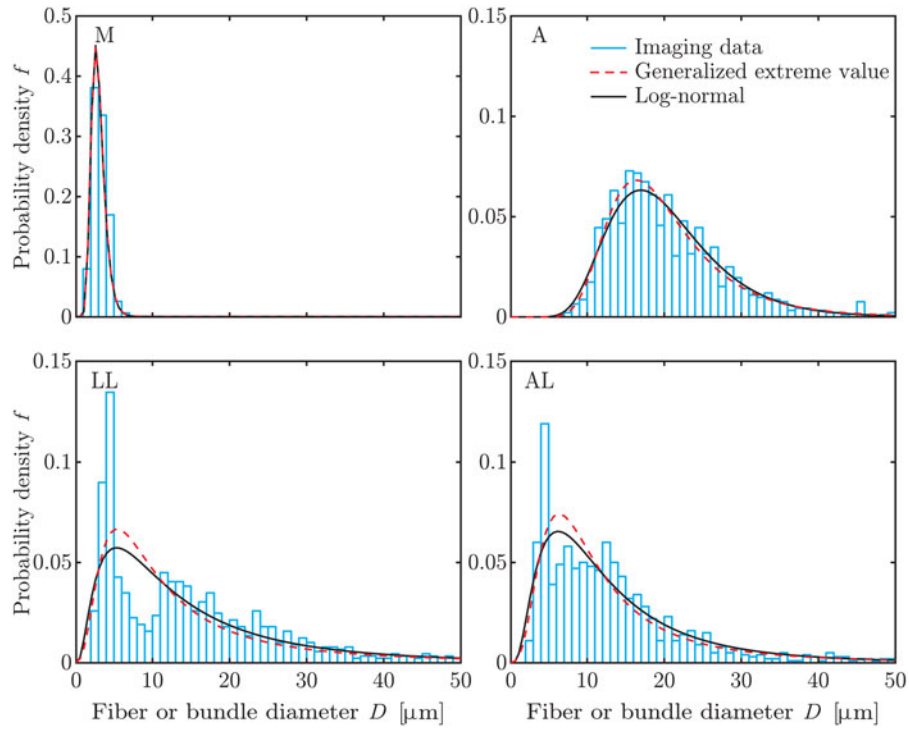

Fig. 7. Distribution of the diameter measurements (blue) for the media (M) and adventitia (A) of healthy aortas as well as the LL and the AL of AAAs together with the log-normal distribution, equation (12) – (solid black curve), and the generalized extreme value distribution, equation (6) – (dashed red curve), fitted to the measurements.

https://doi.org/10.1017/S1431927622000629 Published online by Cambridge University Press

Table 1. Diameter D of the Fibers for the Healthy Media and Fiber Bundles for the Healthy Adventitia, the LL and AL of AAAs.

		D (μm)
Media	Median	3.0
$n = 12$	$[Q_1; Q_3]$	[2.6; 3.6]
Adventitia	Median	21.9
$n = 10$	$[Q_1; Q_3]$	[20.2; 23.9]
Luminal layer	Median	15.7
$n = 6$	$[Q_1; Q_3]$	[5.6; 29.3]
Abluminal layer	Median	14.0
$n = 10$	$[Q_1; Q_3]$	[8.1; 17.7]

n indicates the number of measured samples for the respective layer.

Table 2. Parameters of the Generalized Extreme Value Distribution, Equation (6), on the Diameter D of Fibers of the Healthy Media and Fiber Bundles of the Healthy Adventitia and the LL and AL of AAAs.

Generalized Extreme Value	Media	Adventitia	LL	AL
Log-likelihood	−1,496	−3,051	−3,359	−3,501
Mean	2.98	20.4	21.7	15.2
Variance	0.788	62.2	∞	712
Parameter estimate				
k	−0.054	0.089	0.612	0.434
σ	0.739	5.41	6.46	5.38
μ	2.59	16.8	8.10	8.13

Table 3. Parameters of the Log-Normal Distribution, Equation (12), on the Diameter D of Fibers of the Healthy Media and Fiber Bundles of the Healthy Adventitia as well as the Luminal and Abluminal Layers of AAAs.

Log-Normal	Media	Adventitia	LL	AL
Log-likelihood	−1,496	−3,056	−3,336	−3,497
Mean	2.99	20.4	17.2	14.2
Variance	0.808	54.1	348	149
Parameter estimate				
μ	1.05	2.95	2.45	2.38
σ	0.295	0.350	0.883	0.743

The luminal layer of AAAs showed similar amplitudes as the healthy media, $A_{LL} = 2.4\ \mu$m [2.3; 3.1] ($p = 0.75$). However, they differed significantly ($p = 0.04$) in tortuosity, $T_{LL} = 1.02$ [1.02; 1.04], since the luminal layer of AAA showed more scattered values. Interestingly, the abluminal layer of AAAs showed no significant difference in tortuosity compared to the adventitia, $T_{AL} = 1.27$ [1.03; 1.45] ($p = 0.19$). However, the amplitudes in the abluminal layer of AAAs were significantly smaller, $A_{AL} = 5.8\,\mu$m [2.6; 9.3], compared to the adventitia of healthy tissue ($p < 0.001$). A summary of all measurements can be found in Table 4. Interestingly, the end-point-distance L_0 varied significantly between the adventitia of healthy samples, $L_{0,A} = 39.8\,\mu$m [37.2; 43.9], and the abluminal layer of diseased samples, $L_{0,AL} = 24.2\,\mu$m [22.2; 35.4], with $p = 0.01$, see Table 4 and Figure 10.

In healthy tissues, the tortuosity of the adventitia was clearly higher than that of the media, where mainly straight fibers were seen. The tortuosity of the AL of AAAs was clearly lower compared to the adventitia, while the variability for the LL of AAAs was

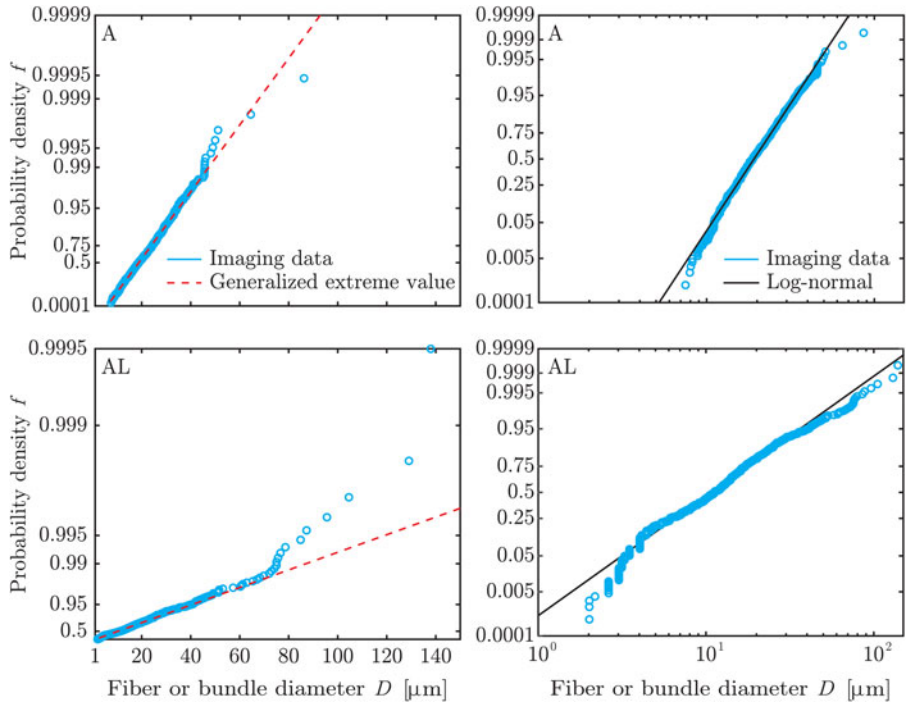

Fig. 8. Probability density plots of the diameter measurements (blue), in logarithmic scale, versus generalized extreme value (dashed red curve) and log-normal (solid black curve) distributions, for the healthy adventitia (A) and the AL of AAAs.

https://doi.org/10.1017/S1431927622000629 Published online by Cambridge University Press

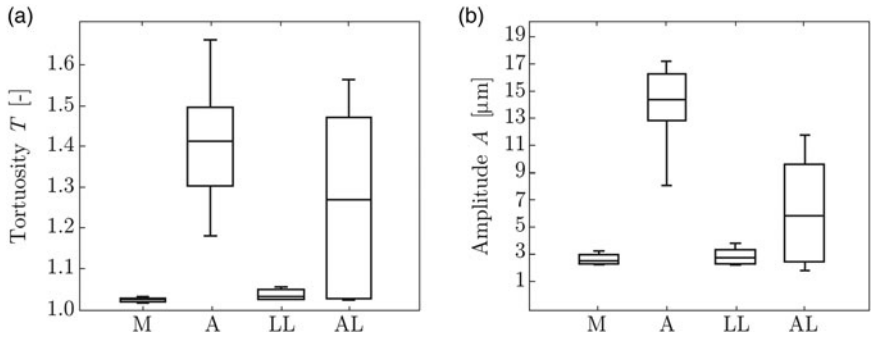

Fig. 9. Box-and-whisker plots for (**a**) the tortuosity and (**b**) the amplitude for the media (M) and adventitia (A) of healthy aortas as well as the LL and the AL of AAAs.

Table 4. Tortuosity T, Amplitude A, and End-Point Distance L_0 for the Media and Adventitia of Healthy Aortas as well as the LL and AL of AAAs.

		T (–)	A (μm)	L_0 (μm)
Media	Median	1.02	2.5	50.4
$n = 12$	$[Q_1; Q_3]$	[1.02; 1.02]	[2.3; 2.8]	[48.7; 53.4]
Adventitia	Median	1.41	14.3	39.8
$n = 10$	$[Q_1; Q_3]$	[1.33; 1.48]	[13.3; 15.6]	[37.2; 43.9]
Luminal layer	Median	1.02	2.4	38.9
$n = 6$	$[Q_1; Q_3]$	[1.02; 1.04]	[2.3; 3.1]	[37.4; 45.4]
Abluminal layer	Median	1.27	5.8	24.2
$n = 10$	$[Q_1; Q_3]$	[1.03; 1.45]	[2.6; 9.3]	[22.2; 35.4]

n indicates the number of measured samples for the respective layer.

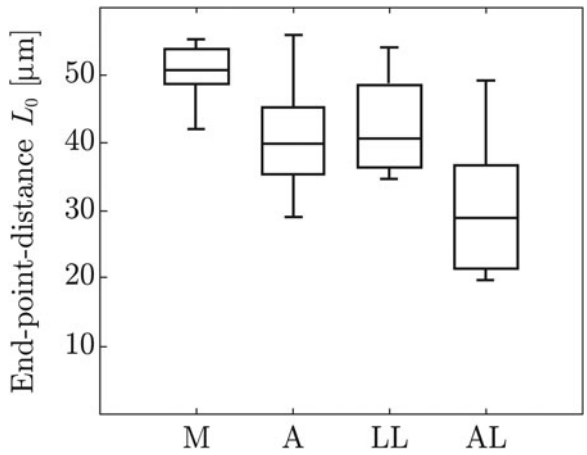

Fig. 10. Box-and-whisker plot of the end-point-distance for the media (M) and adventitia (A) of healthy samples as well as the LL and the AL of AAAs. Note that for straight fibers, the end-point distance depends heavily on the operator and hence should only be looked at for wavy fibers such as fibers in the adventitia and AL of AAAs.

higher compared to the straight medial fibers, see Figure 11a. The amplitudes differed even more clearly. The amplitudes of the healthy adventitia were much higher compared to all other samples. The amplitudes were more similar for AAA tissue, see Figure 11b.

The distribution for the tortuosity measurements turned out to be difficult and only generalized extreme value distribution delivered moderate results, which are shown in Figure 12 and Table 5. In contrary, the straightness parameter showed a good fit to beta and extreme value distributions in the order of preference. The probability histograms together with the distribution fits are shown in Figure 13, whereas the distribution parameters are shown in Tables 6 and 7. Finally, the amplitude measurements showed moderate fits to the gamma and log-logistic distributions with the parameters provided in the Tables 8 and 9. The probability plot accompanied by the fitted distributions is shown in Figure 14.

Collagen Orientation and Dispersion

Collagen fibers in the healthy media were mainly oriented in the circumferential direction, that is, $\alpha_M = \pm 10°$ [7; 21], while in the healthy adventitia more toward the longitudinal direction, $\alpha_A = \pm 53°$ [24; 59], similar to that shown in the previous studies (Schriefl et al., 2012*b*, 2013; Niestrawska et al., 2016; Amabili et al., 2021), despite the fact that the image size was limited to $512 \times 512\ \mu$m (Amabili et al., 2021).

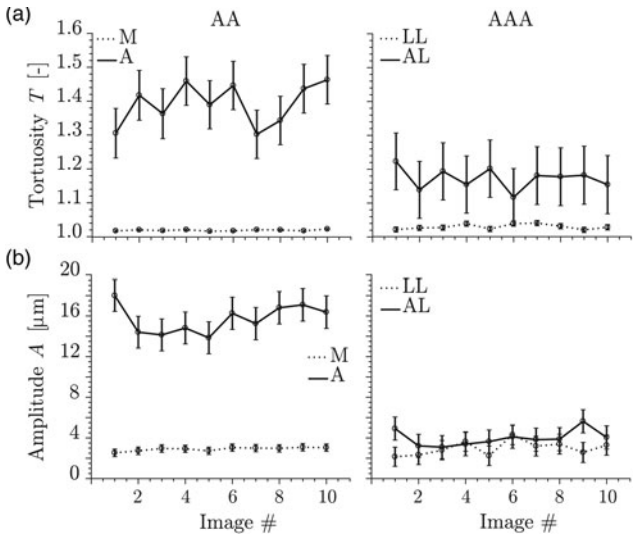

Fig. 11. (**a**) Tortuosity T and (**b**) amplitude A through the thickness of the media (M) and the adventitia (A) of the healthy AA as well as the LL and the AL of the aneurysmal samples (AAA), obtained with ten images for each layer.

https://doi.org/10.1017/S1431927622000629 Published online by Cambridge University Press

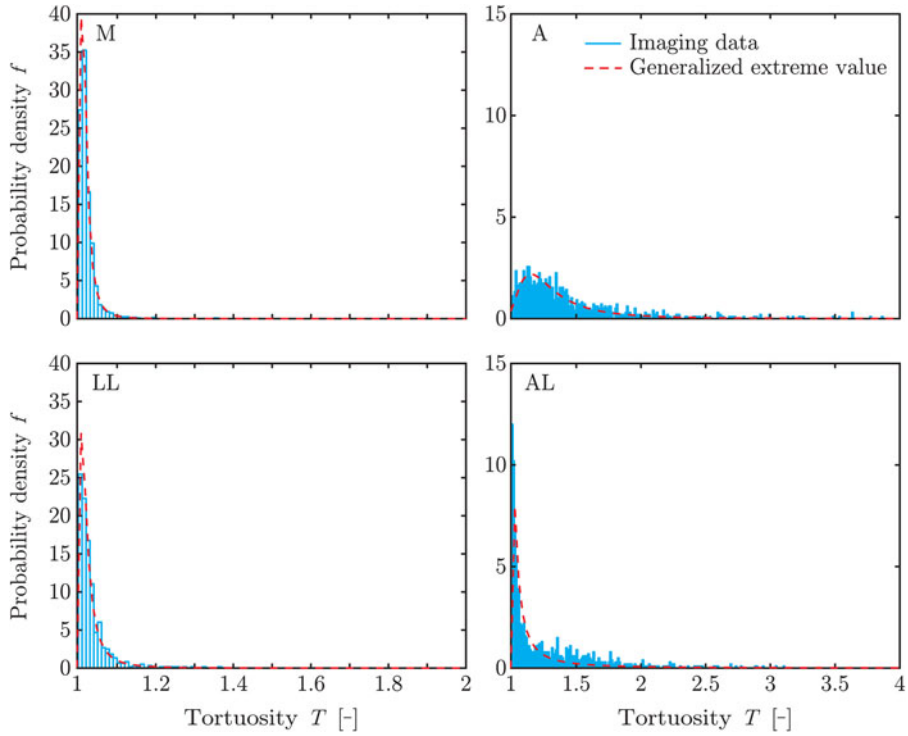

Fig. 12. Distribution of tortuosity measurements (blue) for the media (M) and adventitia (A) of healthy aortas as well as the LL and AL of AAAs together with generalized extreme value distributions (dashed red curve) fitted to the imaging data.

Table 5. Parameters of the Generalized Extreme Value Distribution on the Tortuosity *T* for the Media and Adventitia of Healthy Aortas as well as the LL and AL of AAAs.

Generalized Extreme Value	Media	Adventitia	LL	AL
Log-likelihood	3,593	−98.0	1,443	377
Mean	1.02	1.43	1.04	∞
Variance	<0.001	0.604	∞	∞
Parameter estimate				
k	0.377	0.417	0.571	1.37
σ	0.009	0.180	0.013	0.069
μ	1.01	1.21	1.01	1.04

In addition, the measured values of the dispersion parameters, both in-plane, $\kappa_{ip,M} = 0.188$ [0.166; 0.226] and $\kappa_{ip,A} = 0.266$ [0.222; 0.277], and out-of-plane, $\kappa_{op,M} = 0.465$ [0.458; 0.477] and $\kappa_{op,A} = 0.454$ [0.436; 0.459], were comparable to the results previously reported by Niestrawska et al. (2016). Notably, the medial and adventitial layers of the healthy aortas vary significantly in regard to the orientation ($p = 0.04$) and both in-plane ($p = 0.03$) and out-of-plane ($p = 0.002$) dispersions of the collagen fibers. The parameters obtained are summarized in Table 10.

The luminal layers of AAA samples were even more circumferentially oriented and did not differ significantly from the medias in healthy tissue ($p = 0.55$), with $\alpha_{LL} = \pm 23°$ [9; 46]. The in-plane dispersion of the luminal layer was also not significantly higher than that of the healthy media ($p = 0.08$), with $\kappa_{ip,LL} = 0.249$ [0.201; 0.259]. In addition, the out-of-plane dispersion of the healthy media and the LL of AAA, $\kappa_{op,LL} = 0.472$ [0.458; 0.480], were not significantly different ($p = 0.11$). The AL of AAA did not differ significantly from the adventitia in terms of the mean fiber direction, $\alpha_{AL} = \pm 40°$ [23; 68] ($p = 0.73$), the in-plane dispersion, $\kappa_{ip,AL} = 0.246$ [0.230; 0.295] ($p = 0.73$), and the out-of-plane dispersion, $\kappa_{op,AL} = 0.412$ [0.398; 0.443] ($p = 0.10$). Finally, the AL, compared to the luminal layer, showed no significant difference in all orientation ($p = 0.26$), in-plane ($p = 0.88$), and out-of-plane ($p = 0.06$) dispersion parameters.

Correlations Between Measures of Diameter, Waviness, Orientation, and Dispersion

For all healthy abdominal aortic samples, correlations between the dispersion parameters κ_{ip} and both tortuosity and amplitude could be identified (all p-values < 0.03). The in-plane dispersion was positively correlated with the amplitude ($r = 0.60$, $p = 0.01$) and tortuosity ($r = 0.51$, $p = 0.03$), whereas the out-of-plane dispersion was negatively correlated with both the amplitude ($r = -0.54$, $p = 0.02$) and the tortuosity ($r = -0.55$, $p = 0.02$). In addition, the out-of-plane dispersion was negatively correlated with the diameter ($r = -0.69$, $p = 0.001$), whereas the diameter was positively correlated with the amplitude and tortuosity (both $r = 0.78$, $p < 0.001$).

Aneurysmal samples showed only significant correlations for out-of-plane dispersion with amplitude ($r = -0.54$, $p = 0.04$) and tortuosity ($r = -0.58$, $p = 0.03$). In addition, the p-value for both was higher than the corresponding p-value for the healthy samples. Figure 15 shows scatter plots of the amplitude versus the diameter for healthy and aneurysmal samples.

https://doi.org/10.1017/S1431927622000629 Published online by Cambridge University Press

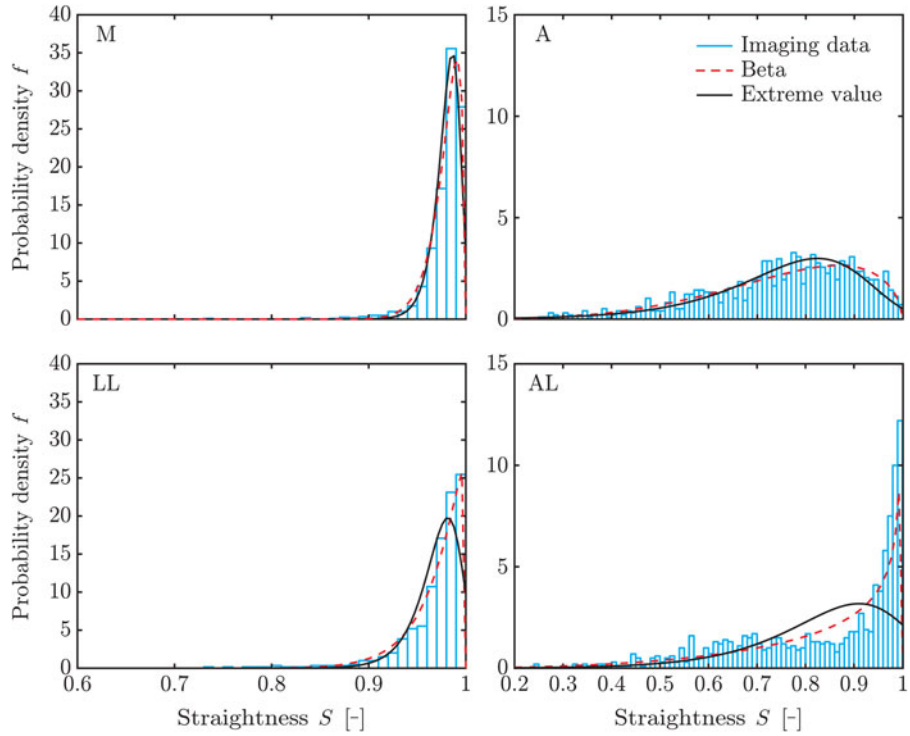

Fig. 13. Distribution of the measurement of the straightness parameter *S* (blue) for the media (M) and adventitia (A) of healthy aortas as well as the LL and the AL of AAAs together with the extreme value distribution (solid black curve) and the beta distribution (dashed red curve) fitted to the imaging data.

Table 6. Parameters of the Beta Distribution of the Straightness Parameter *S* for the Media and Adventitia of Healthy Aortas as well as the LL and AL of AAAs.

Beta	Media	Adventitia	LL	AL
Log-likelihood	3,572	521	1,470	876
Mean	0.979	0.752	0.969	0.838
Variance	<0.001	0.025	<0.001	0.028
Parameter estimate				
α	80.9	4.84	33.5	3.29
β	1.73	1.59	1.09	0.635

Table 7. Parameters of the Extreme Value Distribution on the Straightness Parameter *S* for the Media and Adventitia of Healthy Aortas, and the LL and AL of AAAs.

Extreme Value	Media	Adventitia	LL	AL
Log-likelihood	3,497	499	1,372	514
Mean	0.980	0.753	0.971	0.844
Variance	<0.001	0.025	<0.001	0.022
Parameter estimate				
μ	0.986	0.824	0.982	0.910
σ	0.010	0.123	0.019	0.116

Table 8. Parameters of the Gamma Distribution on the Amplitude *A* for the Media and Adventitia of Healthy Aortas, and the LL and AL of AAAs.

Gamma	Media	Adventitia	LL	AL
Log-likelihood	−2,625	−3,654	−1,154	−2,769
Mean	3.78	19.7	2.80	6.17
Variance	6.11	135	4.07	24.6
Parameter estimate				
α	2.34	2.89	1.92	1.55
β	1.62	6.83	1.45	3.99

Table 9. Parameters of the Log-Logistic Distribution on the Amplitude *A* for the Media and Adventitia of Healthy Aortas, and the LL and AL of AAAs.

Log-Logistic	Media	Adventitia	LL	AL
Log-likelihood	−2,623	−3,669	−1,170	−2,843
Mean	4.02	21.1	3.17	8.10
Variance	22.1	356	33.9	∞
Parameter estimate				
μ	1.12	2.84	0.798	1.54
σ	0.396	0.352	0.449	0.546

Discussion

In this study, differences in collagen fiber diameter and waviness were demonstrated between healthy and aneurysmal abdominal aortas. The limitation of this study is a load-free state of the aortic wall during imaging. Consequently, the differences shown apply to the load-free state and may differ for the *in vivo* state. Considering that the mechanical behavior of an aortic wall changes with aneurysm progression (Niestrawska et al., 2019) and collagen waviness changes with increasing loading (Chow

https://doi.org/10.1017/S1431927622000629 Published online by Cambridge University Press

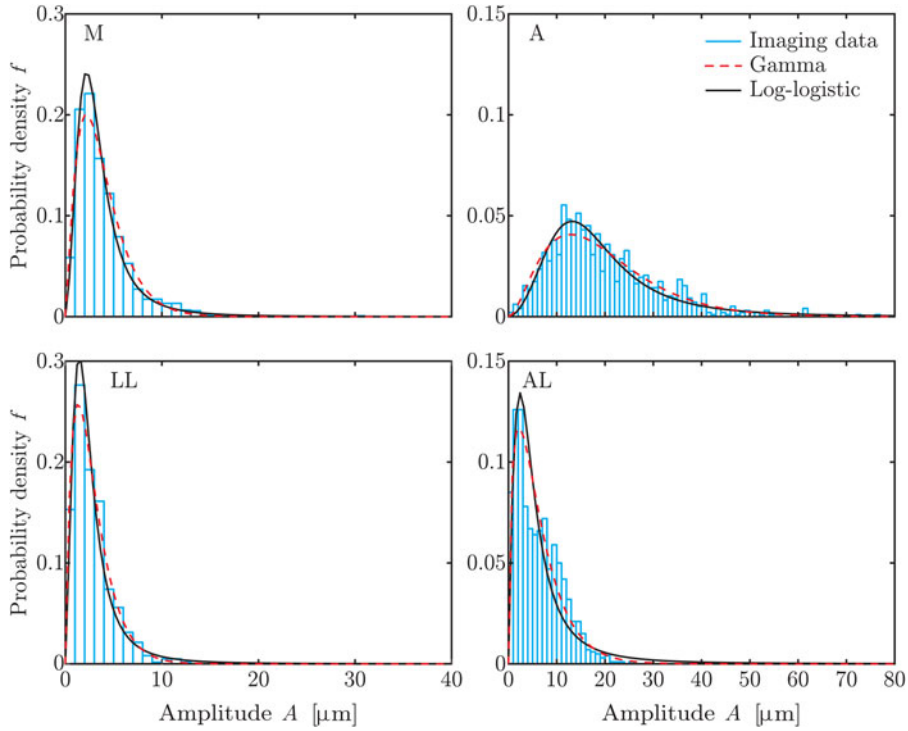

Fig. 14. Distribution of the amplitude measurement (blue) for the media (M) and adventitia (A) of healthy aortas as well as the LL and the AL of AAAs together with the log-logistic distribution (solid black curve) and the gamma distribution (dashed red curve) fitted to the measurements.

Table 10. Dispersion Parameters κ_{ip} and κ_{op} and Mean Fiber Direction α for the Media and Adventitia of Healthy Aortas as well as the LL and AL of AAAs.

		κ_{ip} (–)	κ_{op} (–)	α (°)
Media	Median	0.188	0.465	10
$n = 12$	$[Q_1; Q_3]$	[0.166; 0.226]	[0.458; 0.477]	[7; 21]
Adventitia	Median	0.266	0.454	53
$n = 10$	$[Q_1; Q_3]$	[0.222; 0.277]	[0.436; 0.459]	[24; 59]
Luminal layer	Median	0.249	0.472	23
$n = 6$	$[Q_1; Q_3]$	[0.201; 0.259]	[0.458; 0.480]	[9; 46]
Abluminal layer	Median	0.246	0.412	40
$n = 10$	$[Q_1; Q_3]$	[0.230; 0.295]	[0.398; 0.443]	[23; 68]

n indicates the number of samples measured for the respective layer.

et al., 2014; Krasny et al., 2017; Pukaluk et al., 2021), analysis of collagen waviness in the *in vivo* conditions could be of interest for future studies.

The diameter of the collagen fibers was previously measured by Chen et al. (2011, 2013) in the fresh porcine coronary adventitia, and Pickering et al. (1996) documented diameters on atherosclerotic human samples. The healthy porcine adventitia had a mean fiber diameter of 2.8 μm (Chen et al., 2011, 2013), which is very similar to the healthy human medial fiber diameter of 3.0 μm measured in our study. A comparison between healthy porcine adventitia and healthy human adventitia is not possible because we measured the diameter of clearly formed collagen bundles and not fibers. However, we have observed both fibers and bundles in the aneurysmal adventitia. The fibers of the aneurysmal adventitia were thicker than those reported in healthy porcine samples (Chen et al., 2011, 2013) and healthy human samples from our study, as can be seen from the diameter distribution in Figure 7. The value of the first quartile from the aneurysmal abluminal layer, see Figure 6 and Table 1, is also higher than the diameter of healthy collagen fibers in healthy arterial and aortic samples. This observation of thicker collagen fibers in the aneurysmal abdominal layer has already been pointed out by Niestrawska et al. (2016) and Urabe et al. (2016). In addition, the thicker fibers in the atherosclerotic human adventitia with a mean fiber diameter of 9.2 μm were previously reported by Pickering et al. (1996). This similarity between atherosclerotic and aneurysmal collagen fibers seems plausible, since AAA is often associated with atherosclerosis (Golledge & Norman, 2010).

Rezakhaniha et al. (2012) quantified the waviness of adventitial collagen in the carotid arteries of rabbits using the straightness parameter. Their mean measured straightness parameter was 0.72, which corresponds to the tortuosity of 1.39. Although the samples were taken from different species, in a different location, the tortuosity of collagen from the rabbit carotid adventitia is quite similar compared to the median tortuosity of collagen bundles in the healthy abdominal aortic adventitia that we found (T_A = 1.41). The similarities are not limited to the mean and median values, but extend to the distributions. Rezakhaniha et al. (2012) fitted their data to the beta distribution with estimated $\alpha = 4.47$ and $\beta = 1.76$, which are very similar to $\alpha = 4.84$ and $\beta = 1.59$ for the healthy human aortic adventitia, as analyzed in our study. In addition, the extreme value distribution for the adventitia shows surprisingly similar estimated parameters, that is, μ = 0.800 and $\sigma = 0.133$ for the rabbit's carotid artery versus μ = 0.824 and $\sigma = 0.123$ for the human aorta.

The obtained and quantified values of the geometrical parameters of the collagen fibers and bundles imply a considerable

https://doi.org/10.1017/S1431927622000629 Published online by Cambridge University Press

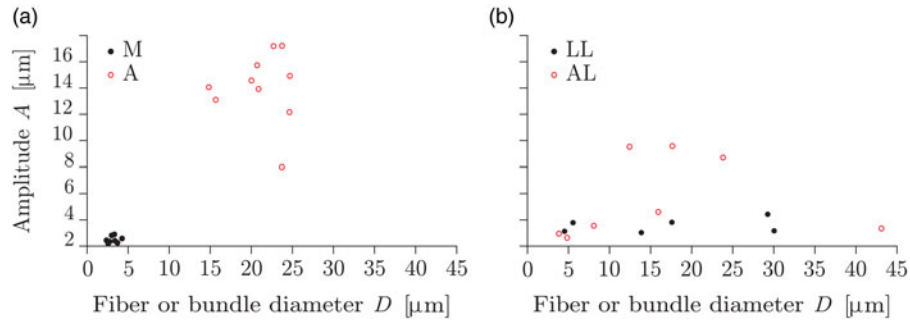

Fig. 15. Relationship between the amplitude *A* and the diameter *D* for (**a**) the healthy media (black solid dots) and the adventitia (red circles) and (**b**) the aneurysmal LL (black solid dots) and the AL (red circles).

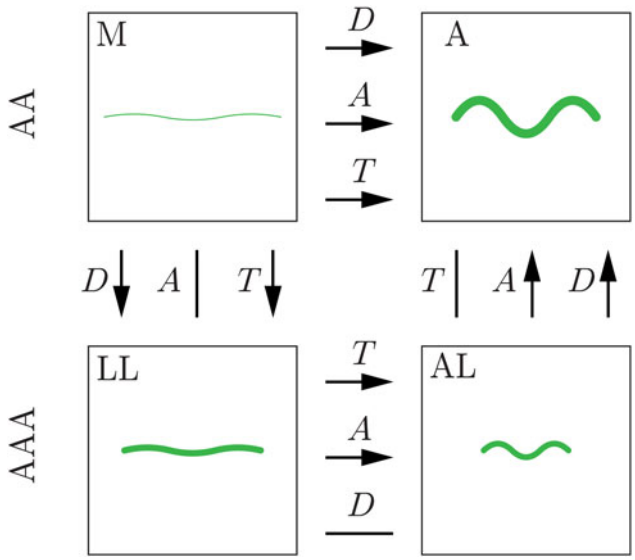

Fig. 16. Summary of the significant differences in diameter *D*, amplitude *A*, and tortuosity *T*, found in the present study. An average collagen fiber is shown schematically (in green) for the media (M) and adventitia (A) of healthy samples (AA) and the LL and the AL of aneurysmal samples (AAA). Significant differences between the layers are indicated by arrows pointing to the layer with the higher parameter value. Straight lines (no arrow) indicate no significant difference between the layers.

remodeling on the micro-scale level. Some significant differences in diameter, amplitude, and tortuosity are summarized in Figure 16. While the diameter of the collagen fibers in the medial layer was significantly different compared to the collagen bundles in the adventitia, there was not much difference between the luminal and abluminal AAA layers. In addition, the collagen diameter showed no difference between the luminal layer and the adventitia, suggesting remodeling of the luminal layer, which tends to the micro-architecture observed in the healthy adventitia. In addition to the collagen diameter, the waviness parameters between the layers of the aneurysmal aortic wall became more similar. As can be seen from Figure 11, the layers become less distinguishable as the amplitude of the collagen wave decreases, especially when looking at the abluminal side. However, the tortuosity of the abluminal layer is still significantly higher than that of the luminal layer. Based on the values of the diameter (Figure 6) and waviness (Figure 7) shown in the box-and-whisker plots, the parameters of the luminal layer were in between the medial and adventitial parameters. The parameters of the AL were also in between the medial and adventitial parameters. This observation suggests that both layers have undergone remodeling; in addition, the aneurysmal aortic wall lost its layer-specific character and tended to become a homogeneous structure.

In contrast, the waviness parameters indicate that the main remodeling occurred on the abluminal side. The end-point distance in the abluminal layer was significantly smaller compared to the healthy adventitia. The amplitude was significantly lower in the aneurysmal abluminal layer than that in the adventitia. These simultaneous changes in both end-point distance and amplitude did not result in a significant difference in tortuosity. Therefore, we hypothesize that the fiber bundles on the abluminal side become more curly and lose their smooth waves to a more curled appearance (see Figure 5 for exemplary images of a healthy adventitia and an aneurysmal AL).

Conclusions

To the best of our knowledge, our comparative study is the first to provide a data set of measurements of collagen diameter and waviness, as well as orientation and dispersion for healthy and aneurysmal abdominal aortas, which can be further used to improve material and multiscale models of aortic walls and aneurysm formation.

Acknowledgments. The authors thank the Institute of Science and Technology Austria in Klosterneuburg for support with SHG imaging. Special thanks go to the contribution of the master's student C. Towler from the University of Glasgow for her work on the integration of MATLAB and ImageJ for the quantification of collagen fibers as well as M. Dalbosco from the Institute of Biomechanics, TU Graz for helpful discussions. Supported by TU Graz Open Access Publishing Fund.

Conflict of interest. The authors declare that they have no known competing financial interests or personal relationships that could have appeared to influence the work reported in this paper.

References

Almutairi Y, Cootes TF & Kadler KE (2015). Tracking collagen fibres through image volumes from SBFSEM. In *Medical Image Understanding and Analysis MIUA 2015*, Lambrou T & Ye X (Eds.) pp. 40–45. Lincoln: BMVA.

Amabili M, Asgari M, Breslavsky ID, Franchini G, Giovanniello F & Holzapfel GA (2021). Microstructural and mechanical characterization of the layers of human descending thoracic aortas. *Acta Biomater* **134**, 401–421.

Annunziata R, Kheirkhah A, Aggarwal S, Hamrah P & Trucco E (2016). A fully automated tortuosity quantification system with application to corneal nerve fibres in confocal microscopy images. *Med Image Anal* **32**, 216–232.

https://doi.org/10.1017/S1431927622000629 Published online by Cambridge University Press

Arivazhagan S, Ganesan L & Priyal SP (2006). Texture classification using Gabor wavelets based rotation invariant features. *Pattern Recognit Lett* **27**, 1976–1982.

Asgari M, Latifi N, Giovanniello F, Espinosa HD & Amabili M (2022). Revealing layer-specific ultrastructure and nanomechanics of fibrillar collagen in human aorta via atomic force microscopy testing: Implications on tissue mechanics at macroscopic scale. *Adv NanoBiomed Res* 2100159. doi: 10.1002/anbr.202100159.

Bode MK, Soini Y, Melkko J, Satta J, Risteli L & Risteli J (2000). Increased amount of type III pN-collagen in human abdominal aortic aneurysms: Evidence for impaired type III collagen fibrillogenesis. *J Vasc Surg* **32**, 1201–1207.

Borgefors G (1986). Distance transformations in digital images. *Comput Vis Graph Image Process* **34**, 344–371.

Brightman A, Rajwa BP, Sturgis JE, McCallister ME, Robinson JP & Voytik-Harbin SL (2000). Time-lapse confocal reflection microcopy of collagen fibrillogenesis and extracellular matrix assembly in vitro. *Biopolymers* **54**, 222–234.

Bullitt E, Gerig G, Pizer SM, Lin W & Aylward SR (2003). Measuring tortuosity of the intracerebral vasculature from MRA images. *IEEE Trans Med Imaging* **22**, 1163–1171.

Carmo M, Colombo L, Bruno A, Corsi FR, Roncoroni L, Cuttin MS, Radice F, Mussini E & Settembrini PG (2002). Alteration of elastin, collagen and their cross-links in abdominal aortic aneurysms. *Eur J Vasc Endovasc Surg* **23**, 543–549.

Chambers JM, Cleveland WS, Kleiner B & Tukey PA (2018). *Graphical Methods for Data Analysis*. Boca Raton, London, New York: CRC Press.

Changoor A, Nelea M, Méthot S, Tran-Khanh N, Chevrier A, Restrepo A, Shive MS, Hoemann CD & Buschmann MD (2011). Structural characteristics of the collagen network in human normal, degraded and repair articular cartilages observed in polarized light and scanning electron microscopies. *Osteoarthr Cartil* **19**, 1458–1468.

Chen H, Liu Y, Slipchenko MN, Zhao X, Cheng JX & Kassab GS (2011). The layered structure of coronary adventitia under mechanical load. *Biophys J* **101**, 2555–2562.

Chen H, Slipchenko MN, Liu Y, Zhao X, Cheng J-X, Lanir Y & Kassab GS (2013). Biaxial deformation of collagen and elastin fibers in coronary adventitia. *J Appl Physiol* **115**, 1683–1693.

Chow M-J, Turcotte R, Lin CP & Zhang Y (2014). Arterial extracellular matrix: A mechanobiological study of the contributions and interactions of elastin and collagen. *Biophys J* **106**, 2684–2692.

Dalbosco M, Carniel TA, Fancello EA & Holzapfel GA (2021). Multiscale numerical analyses of arterial tissue with embedded elements in the finite strain regime. *Comput Methods Appl Mech Eng* **381**, 113844.

D'Amore A, Stella JA, Wagner WR & Sacks MS (2010). Characterization of the complete fiber network topology of planar fibrous tissues and scaffolds. *Biomaterials* **31**, 5345–5354.

Dougherty G & Varro J (2000). A quantitative index for the measurement of the tortuosity of blood vessels. *Med Eng Phys* **22**, 567–574.

Fata B, Carruthers CA, Gibson G, Watkins SC, Gottlieb D, Mayer JE & Sacks MS (2013). Regional structural and biomechanical alterations of the ovine main pulmonary artery during postnatal growth. *J Biomech Eng* **135**, 021022.

Franchini G, Breslavsky ID, Giovanniello F, Kassab A, Holzapfel GA & Amabili M (2022). Role of smooth muscle activation in the static and dynamic mechanical characterization of human aortas. *Proc Natl Acad Sci USA* **119**, e2117232119.

Gandhi RH, Irizarry E, Cantor JO, Keller S, Nackman GB, Halpern VJ, Newman KM & Tilson MD (1994). Analysis of elastin cross-linking and the connective tissue matrix of abdominal aortic aneurysms. *Surgery* **115**, 617–620.

Gasser TC, Gallinetti S, Xing X, Forsell C, Swedenborg J & Roy J (2012). Spatial orientation of collagen fibers in the abdominal aortic aneurysm's wall and its relation to wall mechanics. *Acta Biomater* **8**, 3091–3103.

Gasser TC, Ogden RW & Holzapfel GA (2006). Hyperelastic modelling of arterial layers with distributed collagen fibre orientations. *J R Soc Interface* **3**, 15–35.

Ghazanfari S, Driessen-Mol A, Sanders B, Dijkman PE, Hoerstrup SP, Baaijens FPT & Bouten CVC (2015). In vivo collagen remodeling in the vascular wall of decellularized stented tissue-engineered heart valves. *Tissue Eng Part A* **21**, 2206–2215.

Golledge J & Norman PE (2010). Atherosclerosis and abdominal aortic aneurysm: Cause, response or common risk factors? *Arterioscler Thromb Vasc Biol* **30**, 1075–1077.

Grisan E, Foracchia M & Ruggeri A (2008). A novel method for the automatic grading of retinal vessel tortuosity. *IEEE Trans Med Imaging* **27**, 310–319.

Hayenga HN, Thorne BC, Peirce SM & Humphrey JD (2011). Ensuring congruency in multiscale modeling: Towards linking agent based and continuum biomechanical models of arterial adaptation. *Ann Biomed Eng* **39**, 2669–2682.

Heneghan C, Flynn J, O'Keefe M & Cahill M (2002). Characterization of changes in blood vessel width and tortuosity in retinopathy of prematurity using image analysis. *Med Image Anal* **6**, 407–429.

Holzapfel GA (2008). Collagen in arterial walls: Biomechanical aspects. In *Collagen. Structure and Mechanics*, Fratzl P (Ed.), pp. 285–324. Heidelberg: Springer-Verlag.

Holzapfel GA, Gasser TC & Ogden RW (2000). A new constitutive framework for arterial wall mechanics and a comparative study of material models. *J Elast* **61**, 1–48.

Holzapfel GA, Niestrawska JA, Ogden RW, Reinisch AJ & Schriefl AJ (2015). Modelling non-symmetric collagen fibre dispersion in arterial walls. *J R Soc Interface* **12**, 20150188.

Holzapfel GA & Ogden RW (2018). Biomechanical relevance of the microstructure in artery walls with a focus on passive and active components. *Am J Physiol Heart Circ Physiol* **315**, H540–H549.

Johnson NL, Kotz S & Balakrishnan N (1994*a*). *Continuous Univariate Distributions*, vol. **1**. New York, Chichester, Brisbane, Toronto, Singapore: John Wiley & Sons, Inc.

Johnson NL, Kotz S & Balakrishnan N (1994*b*). *Continuous Univariate Distributions*, vol. **2**. New York, Chichester, Brisbane, Toronto, Singapore: John Wiley & Sons, Inc.

Koch RG, Tsamis A, D'Amore A, Wagner WR, Watkins SC, Gleason TG & Vorp DA (2014). A custom image-based analysis tool for quantifying elastin and collagen micro-architecture in the wall of the human aorta from multi-photon microscopy. *J Biomech* **47**, 935–943.

Koprowski R, Teper SJ, Węglarz B, Wylęgała E, Krejca M & Wróbel Z (2012). Fully automatic algorithm for the analysis of vessels in the angiographic image of the eye fundus. *Biomed Eng Online* **11**, 35.

Krasny W, Morin C, Magoariec H & Avril S (2017). A comprehensive study of layer-specific morphological changes in the microstructure of carotid arteries under uniaxial load. *Acta Biomater* **57**, 342–351.

Li K, Ogden RW & Holzapfel GA (2018). A discrete fibre dispersion method for excluding fibres under compression in the modelling of fibrous tissues. *J R Soc Interface* **15**, 20170766.

Lindeman JH, Ashcroft BA, Beenakker JW, van Es M, Koekkoek NB, Prins FA, Tielemans JF, Abdul-Hussien H, Bank RA & Oosterkamp TH (2010). Distinct defects in collagen microarchitecture underlie vessel-wall failure in advanced abdominal aneurysms and aneurysms in Marfan syndrome. *Proc Natl Acad Sci USA* **107**, 862–865.

Meijering E, Jacob M, Sarria JC, Steiner P, Hirling H & Unser M (2004). Design and validation of a tool for neurite tracing and analysis in fluorescence microscopy images. *Cytometry A* **58**, 167–176.

Menashi S, Campa JS, Greenhalgh RM & Powell JT (1987). Collagen in abdominal aortic aneurysm: Typing, content, and degradation. *J Vasc Surg* **6**, 578–582.

Mencucci R, Marini M, Paladini I, Sarchielli E, Sgambati E, Menchini U & Vannelli GB (2010). Effects of riboflavin/UVA corneal cross-linking on keratocytes and collagen fibres in human cornea. *Clin Exp Ophthalmol* **38**, 49–56.

Myung IJ (2003). Tutorial on maximum likelihood estimation. *J Math Psychol* **47**, 90–100.

Niestrawska JA, Regitnig P, Viertler C, Cohnert TU, Babu AR & Holzapfel GA (2019). The role of tissue remodeling in mechanics and pathogenesis of abdominal aortic aneurysms. *Acta Biomater* **88**, 149–161.

Niestrawska JA, Viertler C, Regitnig P, Cohnert TU, Sommer G & Holzapfel GA (2016). Microstructure and mechanics of healthy and

https://doi.org/10.1017/S1431927622000629 Published online by Cambridge University Press

aneurysmatic abdominal aortas: Experimental analysis and modeling. *J R Soc Interface* **13**, 20160620.

Pickering JG, Ford CM & Chow LH (1996). Evidence for rapid accumulation and persistently disordered architecture of fibrillar collagen in human coronary restenosis lesions. *Am J Cardiol* **78**, 633–637.

Pukaluk A, Wolinski H, Viertler C, Regitnig P, Holzapfel GA & Sommer G (2021). An approach for visualization of the interaction between collagen and elastin in loaded human aortic tissues. In *Proceedings of the Annual Meeting of the Austrian Society for Biomedical Engineering ÖGBMT 2021*, Müller-Putz GR & Baumgartner C (Eds.), pp. 21–24. Graz: Verlag der Technischen Universität Graz.

Rezakhaniha R, Agianniotis A, Schrauwen JTC, Griffa A, Sage D, Bouten CVC, van de Vosse FN, Unser M & Stergiopulos N (2012). Experimental investigation of collagen waviness and orientation in the arterial adventitia using confocal laser scanning microscopy. *Biomech Model Mechanobiol* **11**, 461–473.

Rizzo RJ, McCarthy WJ, Dixit SN, Lilly MP, Shively VP, Flinn WR & Yao JS (1989). Collagen types and matrix protein content in human abdominal aortic aneurysms. *J Vasc Surg* **10**, 365–373.

Roeder BA, Kokini K, Sturgis JE, Robinson JP & Voytik-Harbin SL (2002). Tensile mechanical properties of three-dimensional type I collagen extracellular matrices with varied microstructure. *J Biomech Eng* **124**, 214–222.

Schindelin J, Arganda-Carreras I, Frise E, Kaynig V, Longair M, Pietzsch T, Preibisch S, Rueden C, Saalfeld S, Schmid B, Tinevez JY, White DJ, Hartenstein V, Eliceiri K, Tomancak P & Cardona A (2012). Fiji: An open-source platform for biological-image analysis. *Nat Methods* **9**, 676–682.

Schriefl AJ, Reinisch AJ, Sankaran S, Pierce DM & Holzapfel GA (2012*a*). Quantitative assessment of collagen fiber orientations from 2D images of soft biological tissues. *J R Soc Interface* **9**, 3081–3093.

Schriefl AJ, Schmidt T, Balzani D, Sommer G & Holzapfel GA (2015). Selective enzymatic removal of elastin and collagen from human abdominal aortas: Uniaxial mechanical response and constitutive modeling. *Acta Biomater* **17**, 125–136.

Schriefl AJ, Wolinski H, Regitnig P, Kohlwein SD & Holzapfel GA (2013). An automated approach for three-dimensional quantification of fibrillar structures in optically cleared soft biological tissues. *J R Soc Interface* **10**, 20120760.

Schriefl AJ, Zeindlinger G, Pierce DM, Regitnig P & Holzapfel GA (2012*b*). Determination of the layer-specific distributed collagen fiber orientations in human thoracic and abdominal aortas and common iliac arteries. *J R Soc Interface* **9**, 1275–1286.

Semmlow JL (2004). Fundamentals of image processing: MATLAB image processing toolbox. In *Biosignal and Biomedical Image Processing: MATLAB-Based Applications*, Semmlow JL (Ed.), pp. 279–311. New York: Marcel Dekker.

Sherifova S & Holzapfel GA (2019). Biomechanics of aortic wall failure with a focus on dissection and aneurysm: A review. *Acta Biomater* **99**, 1–17.

Sherifova S & Holzapfel GA (2020). Biochemomechanics of the thoracic aorta in health and disease. *Prog Biomed Eng* **2**, 032002.

The MathWorks Inc. (2021). MATLAB R2021a, Natick, MA, USA.

Thunes JR, Phillippi JA, Gleason TG, Vorp DA & Maiti S (2018). Structural modeling reveals microstructure-strength relationship for human ascending thoracic aorta. *J Biomech* **71**, 84–93.

Towler C (2017). Quantification of fibre waviness in healthy and diseased abdominal aortas. Master's Thesis. University of Glasgow, Biomedical Engineering.

Tsamis A, Krawiec JT & Vorp DA (2013). Elastin and collagen fibre microstructure of the human aorta in ageing and disease: A review. *J R Soc Interface* **10**, 20121004.

Urabe G, Hoshina K, Shimanuki T, Nishimori Y, Miyata T & Deguchi J (2016). Structural analysis of adventitial collagen to feature aging and aneurysm formation in human aorta. *J Vasc Surg* **63**, 1341–1350.

Weisbecker H, Unterberger MJ & Holzapfel GA (2015). Constitutive modelling of arteries considering fibre recruitment and three-dimensional fibre distribution. *J R Soc Interface* **12**, 20150111.

Weisbecker H, Viertler C, Pierce DM & Holzapfel GA (2013). The role of elastin and collagen in the softening behavior of the human thoracic aortic media. *J Biomech* **46**, 1859–1865.

Wu J, Rajwa B, Filmer DL, Hoffmann CM, Yuan B, Chiang CS, Sturgis J & Robinson JP (2003). Analysis of orientations of collagen fibers by novel fiber-tracking software. *Microsc Microanal* **9**, 574–580.

Zeinali-Davarani S, Wang Y, Chow MJ, Turcotte R & Zhang Y (2015). Contribution of collagen fiber undulation to regional biomechanical properties along porcine thoracic aorta. *J Biomech Eng* **137**, 051001.

Ziabari M, Mottaghitalab V & Haghi AK (2009). Application of direct tracking method for measuring electrospun nanofiber diameter. *Braz J Chem Eng* **26**, 53–62.

https://doi.org/10.1017/S1431927622000629 Published online by Cambridge University Press